Structural phase transitions in [(CH3)4P]3M2Cl9 (M = Bi and Sb) hybrid compounds revealed by temperature-controlled Raman spectroscopy and X-ray diffraction

M. Khalfa, A. Oueslati, K. Khirouni, M. Gargouri, A. Rousseau, J.-F. Bardeau, G. Corbel

Journal of Physics and Chemistry of Solids 176 (2023) 111227

Contents lists available at ScienceDirect

Journal of Physics and Chemistry of Solids

Structural phase transitions in $[(CH_3)_4P]_3M_2Cl_9$ (M = Bi and Sb) hybrid compounds revealed by temperature-controlled Raman spectroscopy and X-ray diffraction

M. Khalfa [a,**], A. Oueslati [b], K. Khirouni [a,*], M. Gargouri [b], A. Rousseau [c], J.-F. Bardeau [c], G. Corbel [c,***]

[a] Laboratoire de Physique des Matériaux et des Nanomatériaux Appliquée à l'Environnement, Faculté des Sciences de Gabès cité Erriadh, 6079, Gabès, Tunisia
[b] Laboratoire de Caractérisation Spectroscopique et Optique des Matériaux, Faculté des Sciences, Université de Sfax, B. P. 1171, 3000, Sfax, Tunisia
[c] Institut des Molécules et Matériaux du Mans (IMMM), UMR-6283 CNRS, Le Mans Université, 72085, Le Mans Cedex 9, France

A B S T R A C T

Two phosphonium chlorobismuthate (III) and chloroantimonate (III) crystals have been prepared and their thermal behaviors have been studied by thermal analyses, temperature-controlled Raman spectroscopy and temperature-controlled X-ray diffraction. Refinements of the diffraction pattern, carried out by the Le Bail method, confirm the high purity of both samples. Raman spectroscopy revealed a decomposition of the com-pounds above 250 °C, later confirmed by energy dispersive X-ray (EDX) analysis and X-ray powder diffraction (XRPD). In addition, temperature-controlled Raman spectroscopy and X-ray powder diffraction allowed us to reveal the existence of transitions in the 25–150 °C temperature range, which had previously gone completely unnoticed despite numerous published studies. These transitions are related to reorientations of the tetramethyl phosphonium cations $[(CH_3)_4P]^+$ and rotations of $[M_2Cl_9]^{3-}$ (M = Bi or Sb) dimers in the structure. The rear-rangements of the cationic and anionic entities then change the thermal expansion coefficients measured by diffraction along the trigonal crystallographic axes of the structure.

1. Introduction

Among a large number of hybrid compounds discovered so far, $R_aM_bX_{(3b+a)}$ (R: cations = $((C_nH_{2n+1})_4Y$ where Y= P, N)); M = Sb, Bi and X = Cl, Br, I) compounds has received considerable attention due to its interesting physical (ferroelastic, ferroelectric, piezoelectric) properties [1–5]. These properties are mainly related to the dynamical reor-ientation of the alkyl cations chains and/or to displacements of the M (III) ions within the anionic networks [1,6–8].

The compound with the poly-anionic units $[M_2X_9]^{3-}$ forming two dimensional networks and the one with bioctahedral $[M_2X_{11}]^{5-}$ units in which two $[MX_6]^{3-}$ octahedral are linked together by a bridging halogen atom [3]. Halogenobismuthates ions (Bi (III)) and antimonates ions (Sb (III)) based on elements of groups 15 and 14 (column V), respectively, are well known for their ns^2 electronic lone pair which can be stereo-chemically active or inactive [9,10]. Consequently, the interest of this family of compounds therefore comes not only from its structural di-versity but also from its potential applications in the development of low-cost electronic devices (thin-film transistor, organic-inorganic light-emitting diode) and in terms of conversion of energy in solar cells [11–13].

It should be mentioned that there is a particular interest in the inorganic halide compounds $R_3M_2X_9$, since the discovery of their py-roelectric properties [1]. The study of hybrid compounds based on tetra-alkylphosphonium cations of the general formula $[(C_nH_{2n+1})_4P]$, (where n = 1, 2, 3, 4) revealed several structural phase transitions caused by reorientation dynamics of the cationic groups. According to P. P. Shi et al. [14], $[(CH_3)_4P]FeCl_4$ and $[(CH_3)_4P]FeBr_4$ compounds show a paraelectric–ferroelectric phase transitions, above room temperature (at 362 and 353 K respectively), accompanied by notable dielectric anomalies, reversible polarizations and nonlinear optical (NLO) re-sponses. These transitions can be attributed to the rotations of the

* Corresponding author.
** Corresponding author.
*** Corresponding author.
E-mail addresses: khalfamaryem@gmail.com (M. Khalfa), Kamel.Khirouni@fsg.rnu.tn (K. Khirouni), gwenael.corbel@univ-lemans.fr (G. Corbel).

https://doi.org/10.1016/j.jpcs.2023.111227

cations $[(CH_3)_4P]^+$, which is confirmed by the calculations of the potential energies of rotation.

Among these materials, the compounds $[(CH_3)_4P]_3Bi_2Cl_9$ (PCB) and $[(CH_3)_4P]_3Sb_2Cl_9$ (PCA) exhibit a low temperature paraelestic-ferroelastic phase transition at −122 and −138 °C, respectively [1]. Raman and infrared studies suggested that these transitions are of the order–disorder type (the vibrational states of cations groups change markedly through the phase transitions) [1,4,6–8]. Moreover, these PCA and PCB compounds show a high temperature phase transition at 277 and 261 °C, respectively. The dilatometric and calorimetric studies suggest that these transitions are 'displacive' in nature without any mechanism being identified by Wojtas et al. [1,4,5].

Given the interest in better understanding the phase transition mechanisms of $[(CH_3)_4P]_3Bi_2Cl_9$ (PCB) and $[(CH_3)_4P]_3Sb_2Cl_9$ (PCA) compounds, including the origin of the high temperature phase transition, we studied the structural modifications of these materials by complementary approaches by using temperature-controlled Raman spectroscopy and X-ray diffraction. PCB and PCA compounds will be synthesized by a slow evaporation method at room temperature before studying their thermal behaviours by thermal analyses (TGA-DTA and DSC), temperature-controlled Raman spectroscopy and temperature-controlled X-ray powder diffraction.

2. Experimental details

The synthesis of the $[(CH_3)_4P]_3Bi_2Cl_9$ (PCB) and $[(CH_3)_4P]_3Sb_2Cl_9$ (PCA) compounds were carried out using a preparation procedure reported elsewhere [15–17]. The bismuthate chloride and antimonate chloride were prepared by dissolving Bi_2O_3 or Sb_2O_3 in concentrated hydrochloric acid (HCl, 37%). Then, a stoichiometric quantity of tetramethylphosphonium chloride (purity 98%) was added to these two solutions. The corresponding sequences of chemical reactions are:

$$M_2O_3 + 6\ HCl \rightarrow 2\ MCl_3 + 3H_2O \quad (1)$$

$$3[(CH_3)_4PCl] + 2MCl_3 \rightarrow [(CH_3)_4P]_3M_2Cl_9 \quad (2)$$

where M = Sb or Bi. The solution is left open to the air at room temperature for 5 days, after which bright and transparent crystals begin to appear. Crystals of millimetric size are then isolated, washed with absolute ethanol and kept under standard atmospheric conditions before characterizing them.

The phase purity of the powder was verified by recording X-ray powder diffraction (XRPD) pattern at room temperature on a PANalytical θ/θ Bragg-Brentano Empyrean diffractometer ($CuK\alpha_{1+2}$ radiations) equipped with the PIXcel^{1D} detector. XRPD pattern was collected at room temperature in the [5°–100°] scattering angle range, with a 0.0131° step size, for a total acquisition time of 7 h 30. Thermal stability in air of the as-prepared powder was studied by temperature-controlled X-ray powder diffraction. XRPD patterns were recorded on the same diffractometer between 25 and 130 °C (heating rate of 10 °C/min, temperature stabilisation for 20 min, cooling rate of 60 °C/min, and air flow of 40 mL/min) by using an XRK 900 Anton Paar reactor chamber. The sample was deposited on the sieve (pore size Φ = 0.2 mm) of the open sample holder cup, both made of glass ceramic Macor®, thus allowing air to flow through the sample. For each temperature, the XRPD pattern was collected in the [5°–55°] scattering angle range, with a 0.0131° step size, for a total acquisition time of 120 min. The refinements of the XRPD pattern were carried out by the Le Bail method [18] of the Fullprof program [19].

The differential scanning calorimetry (DSC) measurement was performed using PerkinElmer DSC-7 instrument rate of 5 °C mn^{-1}. It was carried out at two successive heating and cooling runs over a temperature range of 25–300 °C in order to identify the precise phase transition temperature.

The thermogravimetric and differential thermal analysis were simultaneously performed on raw powders of PCA and PCB with a TGA/DTA Q600 SDT TA Instruments apparatus (Pt crucibles, α-Al_2O_3 as a reference) under air flow (100 ml/min) from the room temperature (RT) to 270 °C range (heating/cooling rate of 5 °C/min).

A first series of Raman measurements was carried out on PCB and PCA crystals in the wavenumber range 10–3500 cm^{-1} at 25 °C and heated to 250 °C, then a second series on the temperature range 25–130 °C. The spectra were recorded with a HORIBA Jobin-Yvon T64000 Raman spectrometer equipped with a single monochromator (600 gratings per mm) coupled to a nitrogen cooled front-illuminated charge-coupled device (CCD) detector. The spectra were collected in backscattering geometry under a BX41 Olympus microscope equipped with aMSPlan50x (N.A. 0.55) objective focusing the incident wavelength radiation at 514.5 nm of an argon–krypton ion laser (Innova, Coherent, France). During the experiment, the laser power was less than 2 mW on the sample and the Raman spectra were systematically recorded twice with an integration time of between 40 and 60s. Acquisition and basic analysis of spectra (determination of peak positions and full width at half maximum (FWHM) of the Raman bands using Gaussian fitting functions) have been performed using the LabSpecV5.25 (Jobin-Yvon, Horiba Group, Kyoto, Japan) software.

Confocal Raman mapping 100 × 100 μm^2 area (2D map step size of around 5 μm) was performed at room temperature on a crystal of PCA and PCB heated at 270 °C for 72h. The spectra were recorded using a WITec Alpha 300R confocal Raman spectrometer (WITec GmbH, Ulm Germany) equipped with both a RayShield Coupler and a 600 gmm^{-1} grating blazed at 500 nm and a thermically Peltier-cooled Si-based CCD front-illuminated detector (Andor, Oxford Instrument, Belfast, Ireland). Raman scattered signals were collected under a microscope equipped with a Zeiss EC Epiplan-Apochromat Dic 50x (numerical aperture of 0.95) focusing the 532 nm line of a solid-state sapphire laser (Coherent INC., Santa Clara, USA) with a laser power of 2mW on the sample and integration times set at 2s. The spectral analysis was performed using the WITec Project FIVE plus software (version 5.248, WITec GmbH, Germany) and in particular the True Component Analysis (TCA). This dedicated tool of the WITec Project FIVE plus software allows both identifying pixels of a map with similar spectral features and providing these spectral characteristics (i.e. similar chemical response) in an intensity distribution image. Let us note that before analysis, spectral raw data were baseline corrected and pre-processed by removing the cosmic rays.

The surface morphology of PCB and PCA powder sample was observed by a field emission scanning electron microscope (SEM) using a JEOL JSM-6510LV microanalysis. An OXFORD Energy Dispersive X-ray Spectrometer (EDS) coupled to the microscope was also used to verify the presence of chemical elements in the crystals. Before analysis, small crystals were deposited on a carbon tape and a thin film of gold was sprayed on them.

3. Results and discussion

3.1. X-ray powder diffraction analysis

A portion of the millimetre-sized crystals have been crushed into micrometric powder in order to verify, by X-ray powder diffraction (XRPD), the homogeneity of the two compounds. A refinement of the XRPD pattern (for each sample), collected at room temperature, was carried out by the Le Bail method using the trigonal cell parameters and the *P31c* (n°159) space group reported in Ref. [1]. Fig. 1 shows the observed, calculated, and difference diffraction patterns for PCB and PCA. All Bragg peaks were successfully indexed and satisfactorily fitted using this crystallographic data, thus confirming the high purity of both samples. The conventional reliability factors of the refinement are R_p = 6.47%, $R_{\omega p}$ = 6.77%, R_{exp} = 1.94% for PCB and R_p = 8.09%, $R_{\omega p}$ = 7.81%, R_{exp} = 2.68% for PCA. The trigonal cell parameters (a = 9.5030 (4) Å, c = 22.3276(9) Å for PCB and a = 9.4658(5) Å, c = 22.20(1) Å for PCA) are in good agreement with those determined from XRD data

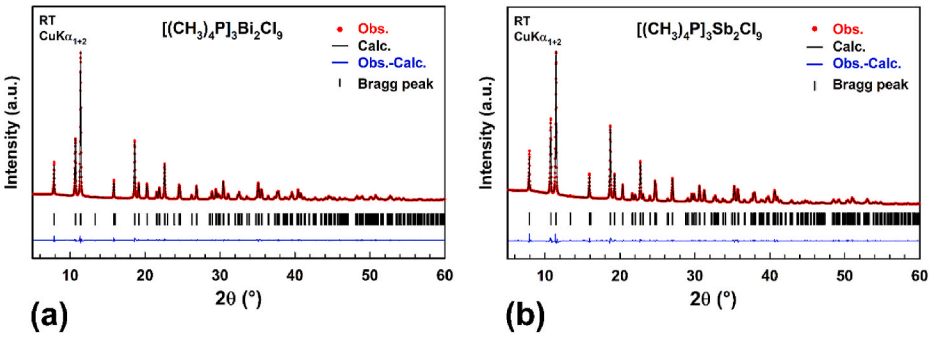

Fig. 1. Comparison of the observed diffraction patterns (red dots) with the patterns calculated by the Le Bail method (black lines) for $[(CH_3)_4P]_3Bi_2Cl_9$ (PCB) (a) and $[(CH_3)_4P]_3Sb_2Cl_9$ (PCA) (b) compounds. Vertical markers give Bragg peak positions of the space group *P 31c* (No.159).

collected on a single crystal of PCB and PCA in the literature [1].

In the crystal structure of both PCB and PCA compounds, each tetramethyl phosphonium $[(CH_3)_4P]^+$ cation has one of its P–C bonds oriented along the threefold axis of the crystal structure (Fig. 2). Two $[MCl_6]^{3-}$ octahedral (M = Bi or Sb) share one of their triangular faces to form isolated dimers of $[M_2Cl_9]^{3-}$ (Fig. 2). Each organic cation is surrounded by three dimers arranged around the threefold axis (Fig. 2). With such an arrangement, three carbon atoms of the $[(CH_3)_4P]^+$ cation interact directly with the chlorine atoms shared between two $[MCl_6]^{3-}$ octahedra (each carbon thus has two first neighbor chlorine atoms at distances d_2 and d_3, respectively), while the fourth carbon atom located on the threefold axis only interacts with the chlorine atoms of one of the triangular faces left free (all atoms at the same distance d_1), as indicated by the grey dashed lines in Fig. 2. Thereby, the methyl groups of each tetramethyl phosphonium $[(CH_3)_4P]^+$ cation have two different chemical environments.

3.2. Thermal analysis

The DSC curves of PCB and PCA compounds recorded upon heating and cooling at 5°Cmin^{-1} are displayed in Fig. 3 (a) and **(b)**, respectively. For each compound, one endothermic peak and one exothermic peak, both of small intensity, are detected on heating and cooling, respectively (temperatures read on the top of the peak: 269/258 °C for PCB and 256/254 °C for PCA). These phenomena are completely reproducible since these peaks are also detected on the second heating/cooling run. The

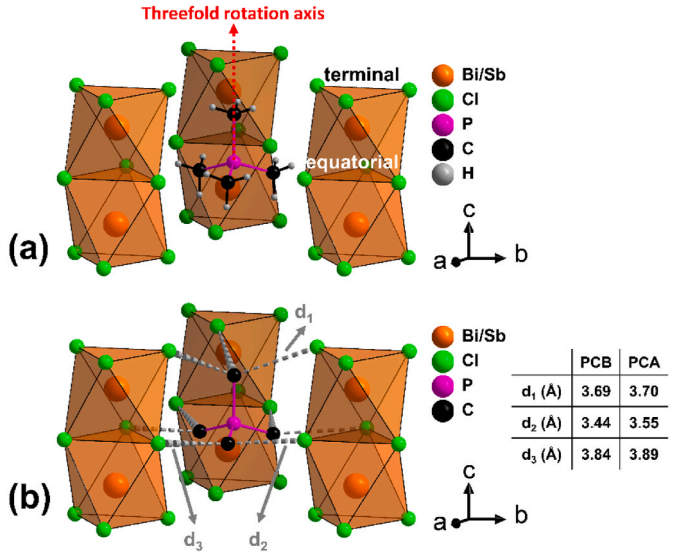

	PCB	PCA
d_1 (Å)	3.69	3.70
d_2 (Å)	3.44	3.55
d_3 (Å)	3.84	3.89

Fig. 2. Structural representation of $[(CH_3)_4P]_3Bi_2Cl_9$ (PCB) and $[(CH_3)_4P]_3Sb_2Cl_9$ (PCA) compounds.

associated entropy value for PCB and PCA are $\Delta S = 2.09$ Jmol^{-1}K^{-1} and $\Delta S = 1.89$ Jmol^{-1}K^{-1}, respectively.

Fig. 4 displays the TGA and DTA curves of the PCB and PCA samples recorded upon heating and cooling. For both compounds, no weight loss is measured from RT to 270 °C indicating that the sample is presumably thermally stable in this temperature range. No endothermic and exothermic peaks appear on the DTA curve upon heating and cooling, reflecting the lower sensitivity of DTA, compared to DSC, to detect such weak signals. So, the nature of the peaks that appears on the DSC curve on heating and cooling cycles is still unclear. Wojtas et al. [1] postulated that this high temperature phase is displacive in nature but gave no experimental evidence for this. In order to identify the nature of this high temperature transition, Raman spectra were recorded in the wavenumber range 10–3500 cm^{-1} over the temperature range 180–250 °C. XRPD pattern and scanning electron microscope (SEM) were carried out after heating the sample up to 270 °C.

3.3. Thermal behavior above 250 °C

3.3.1. Raman analysis

The Raman spectra of PCB and PCA crystals at 25 and heated at 250 °C are shown in Fig. 5. At room temperature, the assignment of the vibrational modes (Table 1) is based on the comparison with similar compounds in literature [4,20–23]. The bands observed in the 50-400 cm^{-1} wavenumber range can be attributed to the vibrational modes of $[M_2Cl_9]^{3-}$ anions (Table S1) and the bands above 400 cm^{-1} are related to the vibrational modes of cationic $[(CH_3)_4P]^+$ cations. After heating the samples up to 250 °C additional broad bands near 1600 cm^{-1} appear; these bands are commonly attributed to the stretching modes of graphitic carbon. At 250 °C, a decrease in the intensity of the peaks of the stretching modes of (CH_3) is also observed for the PCB and the almost total disappearance of these bands for the PCA compound. The presence of graphitic carbon clearly shows that a decomposition process must have taken place on the surface of PCB and PCA crystals when they are heated above 250 °C. To identify the decomposition products, we then decided to characterize each compound after a long heating process above 250 °C by Raman mapping, SEM-EDX analysis and X-ray powder diffraction.

3.3.2. Raman mapping

Fig. 6 shows a Raman mapping based on 400 spectra recorded at ambient temperature in 100 × 100 μm^2 area of PCB crystal surface after heating 72h at 270 °C. Although a large part of the material was modified (easily visible under an optical microscope by its change in surface state), a specific area was chosen to perform the Raman mapping because it remained a small area not modified by temperature. A True Component Analysis (TCA) was used to identify spectral components that are most prevalent in the dataset. The average spectra, which can be extracted from the components, are then helpful to identify and localize different molecular structures. The blue-coded spectral signature

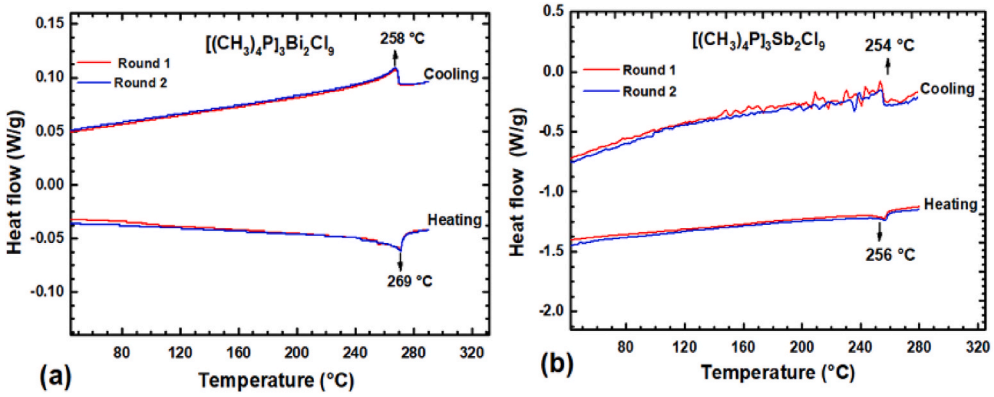

Fig. 3. DSC curve of $[(CH_3)_4P]_3Bi_2Cl_9$ (PCB) (a) and $[(CH_3)_4P]_3Sb_2Cl_9$ (PCA) (b) compounds recorded during heating and cooling.

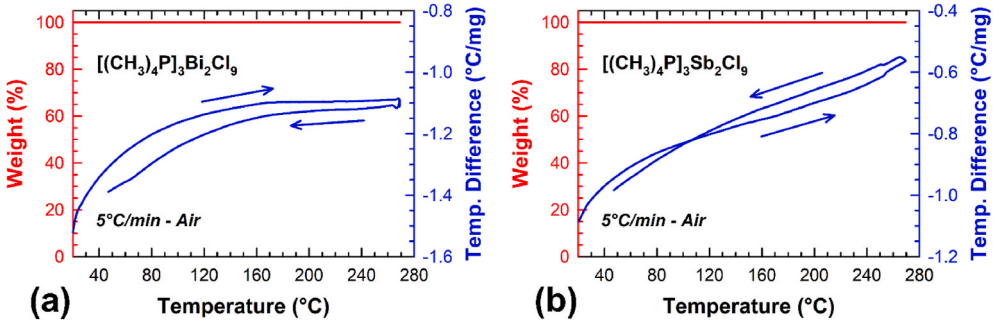

Fig. 4. Thermogravimetric (red) and differential thermal (blue) curves recorded during heating and cooling of $[(CH_3)_4P]_3Bi_2Cl_9$ (PCB) (a) and $[(CH_3)_4P]_3Sb_2Cl_9$ (PCA) (b) powders in air.

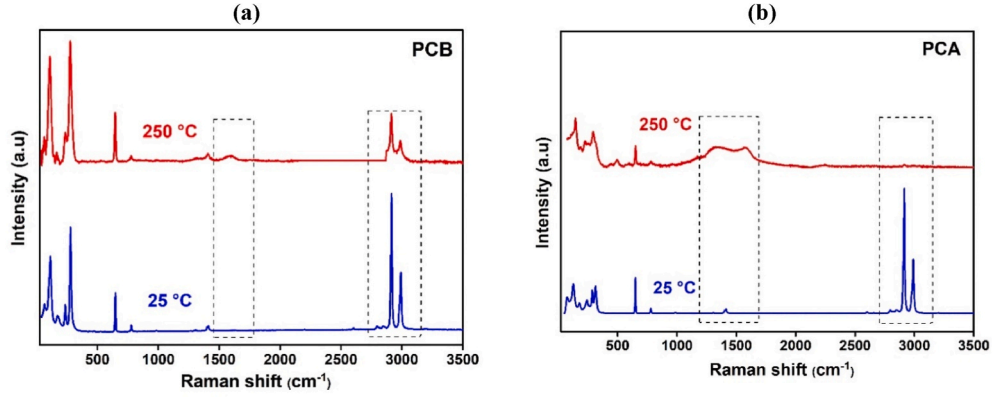

Fig. 5. Raman spectra of $[(CH_3)_4P]_3Bi_2Cl_9$ (PCB) (a) and $[(CH_3)_4P]_3Sb_2Cl_9$ (PCA) (b) compounds at 25 and 250 °C.

corresponds to the PCB crystal not affected by heating (Fig. 6b). The red-coded spectral signature is different from that of the PCB crystal (Fig. 6c). The intense bands at 142 and 199 cm^{-1} can be attributed respectively to A_{1g} internal Bi–Cl stretching mode and E_g internal Bi–Cl stretching mode of BiOCl compound (with space group D^7_{4h}) [24,25], which is in total agreement with diffraction results (rectangle in Fig. 8a). This attribution is also consistent with the presence of a very weak intensity band at 394 cm^{-1}, due to the motion of oxygen atoms. The presence of weak bands at 107, 232 and 276 cm^{-1} (assigned to PCB crystal not affected by heating) in the red-coded spectrum confirms, as shown by X-ray diffraction (Fig. 8), that the thermal decomposition is not complete. Let us note that the absence of other vibrational modes on the spectrum does not allow the identification of other bismuth oxychlorides of different stoichiometry or bismuth oxides (Bi_2O_3 or Bi_2O_5).

A Raman mapping was also carried out on the PCA crystal surface after heating 72h at 270 °C (Fig. 7). Concomitantly, the CH stretching bands decrease very strongly and three bands at 194, 402 and 455 cm^{-1} appear which can be attributed to the bending and stretching vibration of the Sb–O bonds in Sb_2O_4 [26], compound indeed identified by diffraction (rectangle in Fig. 8b).

Considering the decomposition of the compounds above 250 °C, it may be surprising that no weight loss is detected on the thermogravimetric curves displayed in Fig. 4. Nevertheless, due to the heating rate of 5 °C/min and the absence of an isothermal plateau at 270 °C during the thermogravimetric analyses, it can the considered that the time during which the samples are heated above 250 °C is too short to cause their total decomposition and therefore measure the associated weight losses.

Accordingly, the ageing study of PCA and PCB crystals carried out at 270 °C for 3h or 72h clearly demonstrates that the endothermic peak detected by DSC for each compound is associated with its decomposition

Table 1
Band assignment of Raman spectra of $[(CH_3)_4P]_3Bi_2Cl_9$ (PCB) and $[(CH_3)_4P]_3Sb_2Cl_9$ (PCA).

Raman position (cm^{-1}) of PCB	Vibration assignments	Raman position (cm^{-1}) of PCA	Vibration assignments
$[Bi_2Cl_9]^{3-}$		$[Sb_2Cl_9]^{3-}$	
68	Lattice mode	78	Lattice mode
116	δ (BiCl)	126	δ (SbCl)
182	$\nu_{18}(BiCl_{equatorial})$	178	$\nu_{18}(SbCl_{equatorial})$
–	–	241	$\nu_2(SbCl_{equatorial})$
240	$\nu_{15}(BiCl_{terminal})$	287	$\nu_{15}(SbCl_{terminal})$
282	ν_1 $(BiCl_{terminal})$	314	ν_1 $(SbCl_{terminal})$
$[(CH_3)_4P]^+$		$[(CH_3)_4P]^+$	
651	ν_s (C_4P)	649	ν_s (C_4P)
782	ν_{as} (C_4P)	781	ν_{as} (C_4P)
1411	δ_{as} (CH_3)	1402	$\delta_{as}(CH_3)$
1415	δ_{as} (CH_3)	1413	$\delta_{as}(CH_3)$
2798	–	2796	–
2851	–	2851	–
2911	ν_s (CH_3)	2905	ν_s (CH_3)
2919	ν_s (CH_3)	2914	ν_s (CH_3)
2982	ν_{as} (CH_3)	2977	ν_{as} (CH_3)
2994	ν_{as} (CH_3)	2990	ν_{as} (CH_3)

rather than with a displacive structural phase transition, as postulated by Wojtas et al. [1].

3.3.3. SEM-EDX analysis

During Raman experiments, we observed that the surface goes from a reflective state to a much more diffusive state from 250 °C. In order to understand this surface phenomenon, one single crystal of each compound was heated at 270 °C for 3h and then studied by a scanning electron microscope (SEM), coupled with the energy dispersive X-ray (EDX). Figs. S1a and S1b show the SEM images and EDX elemental mappings and EDX spectra of PCA and PCB crystal before and after heating.

The SEM micrograph observed before heating reveals smooth surfaces with small fragments of other crystals. After heating, crystal surfaces are rougher with grey and black areas (Fig. S1a and **S1b)**. From the elemental analyses, we notice that the percentage oxygen increases for both crystals after heating. Although the percentage of carbon is skewed due to the use of carbon tape to stick the sample to the holder, carbon also covers the crystal surface. The carbon at the crystal surface must probably be in an amorphous form (black carbon) since it is not visible on the XRPD pattern (see hereafter). A significant percentage of oxygen is also present in the samples thus leading to a reduction in the Bi/Cl and Sb/Cl ratios of the PCB and PCA compounds, respectively. SEM and EDX results confirm the partial decomposition of PCB and PCA and show that a surface oxidation also occurs up on heating to 270 °C in air. Because this oxidation can lead to either oxychlorides or pure oxides, X-ray powder diffraction was used to identify the products formed.

3.3.4. X-ray powder diffraction

In order to study the structural modifications of the PCB and PCA compounds above 250 °C, XRPD patterns were collected at room temperature after heating the powders at 270 °C under air for 72 h (Fig. 8). When compared with the XRPD pattern of the raw PCB sample, the long heating caused many peaks to appear alongside those attributed to the PCB phase (Fig. 8a), only some of which can be attributed to BiOCl (10, 26, 33 and 34°, JCPDS card n°98-007-4502 [27]). The PCB sample partially decomposes during the prolonged heating to 270 °C. In Fig. 8b, the thermal decomposition of PCA is, in contrast, complete since only broad diffraction peaks of Sb_2O_4 (JCPDS card n°98-000-4109) is detected on the XRPD pattern collected on the powder heated at 270 °C for 72 h.

3.4. Thermal behavior in the range 30–130 °C

In order to probe the thermal behavior of both compounds in the temperature range 30–130 °C, temperature-controlled Raman

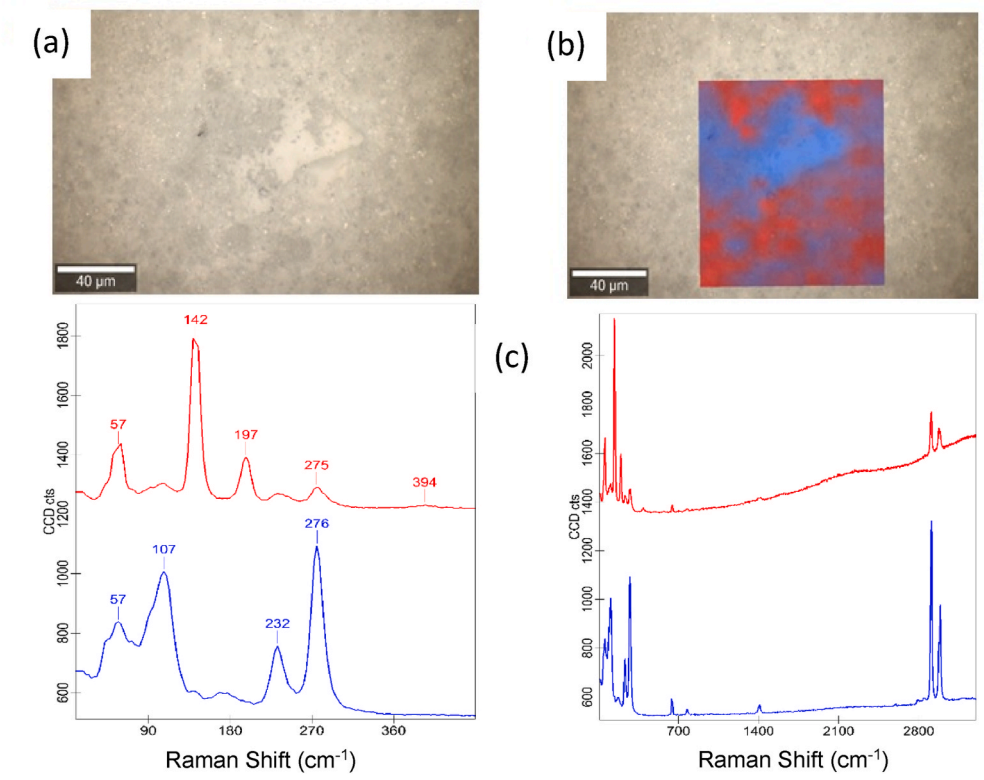

Fig. 6. (a) and (b) Raman mapping recorded at ambient temperature in 100 × 100 μm^2 area of $[(CH_3)_4P]_3Bi_2Cl_9$ (PCB) crystal surface heated 72h at 270 °C. (c) Raman spectra of (PCB) after heating to 270 °C.

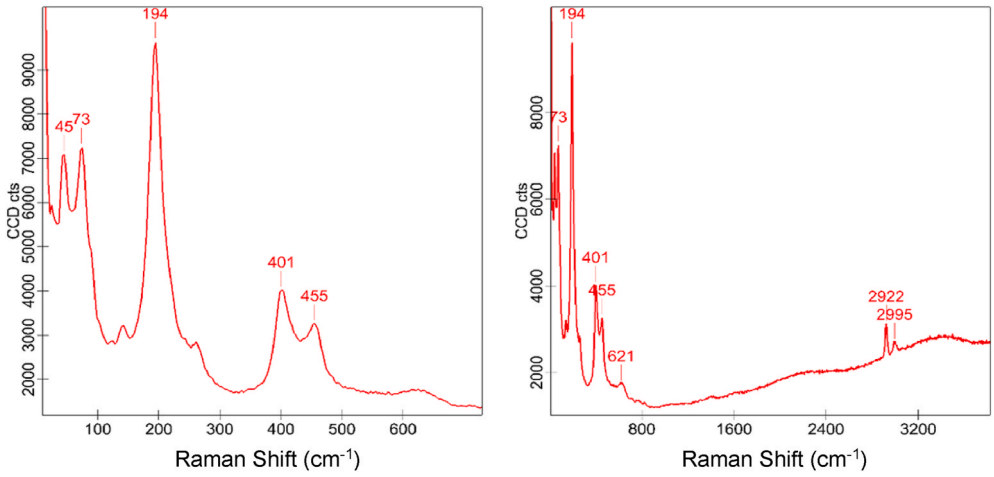

Fig. 7. Raman spectra of $[(CH_3)_4P]_3Sb_2Cl_9$ (PCA) powder, heated at 270 °C.

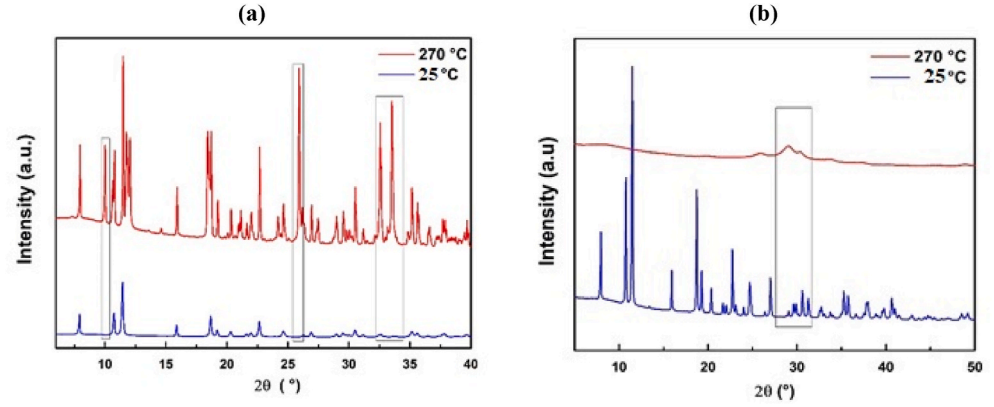

Fig. 8. X-ray diffraction diagram of raw powder of $[(CH_3)_4P]_3Bi_2Cl_9$ (PCB) (a) and $[(CH_3)_4P]_3Sb_2Cl_9$ (PCA) (b) compounds heated 72h at 270 °C.

spectroscopy and XRPD were used.

3.4.1. *Raman spectroscopy analysis*

Raman spectroscopy is one of the powerful tools to study hybrid compounds and reveal phase transitions caused by reorientations of organic entities in the crystal structure [28–32]. Raman spectra of PCB and PCA compounds, collected in the temperature range 30–130 °C, are presented in Figs. 9 and 10, respectively. For more clarity, only selected

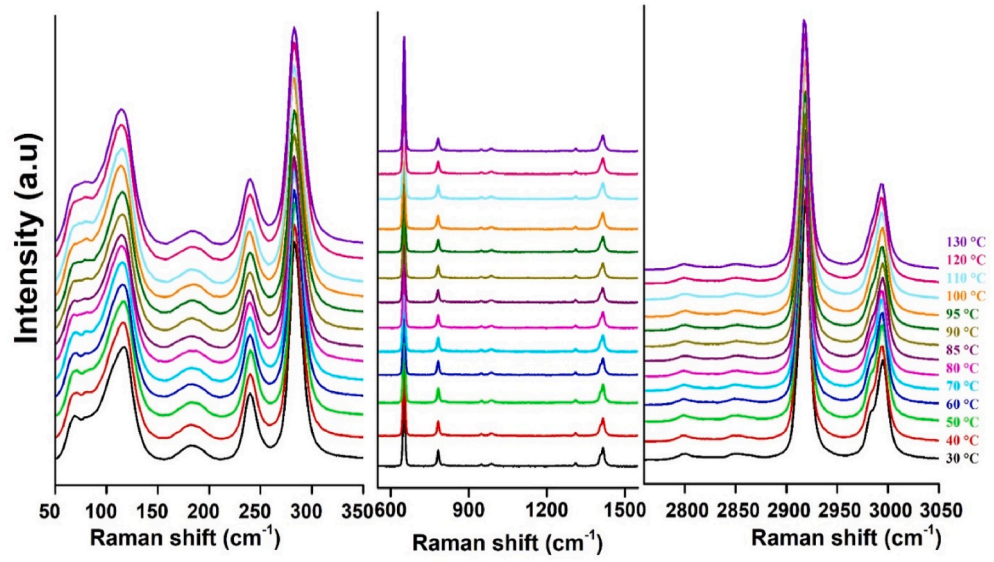

Fig. 9. Temperature evolution of the Raman spectra of $[(CH_3)_4P]_3Bi_2Cl_9$ (PCB) compound in the temperature range 30 °C–130 °C for selected spectral ranges [50-350 cm^{-1}], [500-1550 cm^{-1}] and [2750-3050 cm^{-1}].

spectra were shown in the wavenumber ranges 50-350 cm^{-1}, 550-1550 cm^{-1}, 2750-3050 cm^{-1}. A careful analysis of these spectra makes it possible to observe small variations in terms of positions and half-widths of bands in the temperature range 30–130 °C. Fig. S2 shows an example of deconvolution of the spectrum of PCA compound recorded at 30 °C in the 50–400, 600–1500 and 2750–3150 cm $^{-1}$ spectral ranges.

3.4.1.1. PCB compound. In order to verify whether a phase transition (not detected by thermal analysis) is connected to a change in the dynamical state of the anions and the cations, we presented in Fig. 11 the temperature dependence of the position and the full width at half maximum (FWHM) for the most intense vibrational bands of PCB compound.

The vibration modes of cationic $[(CH_3)_4P]^+$ parts are sensitive indicators to phase transitions. As previously mentioned in the XRPD analysis, PCB compound exhibits two different chemical environments for the methyl group of the tetramethyl phosphonium cation $[(CH_3)_4P]^+$ (Fig. 2). This results in a splitting of the symmetric and asymmetric (CH_3) stretching vibration modes (ν_s and ν_{as}, respectively) with relative integrated intensities in the ratio 1 to 3, as expected. So, the more intense bands at 2919 and 2994 cm^{-1} are assigned respectively to the symmetric and asymmetric stretching vibrations of methyl group in interaction with the equatorial chlorine atoms at distances d_2 and d_3 (Fig. 2) and the bands located at 2911 and 2982 cm^{-1} to the symmetric and asymmetric stretching vibrations of methyl group [20] in interaction with the terminal chlorine atoms at distance d_1 (Fig. 2). In the following, we studied the behavior of all these vibration modes with temperature.

The bands at 2911, 2919, 2982 and 2994 cm^{-1}, shift about 1 cm^{-1} after 80 °C (Fig. 11c) but the evolution of their widths shows a change in slope between 70 and 80 °C, suggesting local changes in the interactions of hydrogen with chloride anions after 70 °C (Fig. 11f). As a consequence, the stretching vibration band of C–P bonds within the tetrahedron C_4P starts broadening from 70 °C (Fig. 11e). The bands at 1412 and 1415 cm^{-1}, associated to CH_3 bending vibration [20], move at 80 °C towards lower wavenumber with a broadening of the band of 1 cm^{-1} (Fig. 11b) similarly to what can be observed for the symmetric $\nu_s(C_4P)$ and asymmetric $\nu_{as}(C_4P)$ stretching vibrations (Fig. 11 e). The phase transition at around 70–80 °C would result from a local reorientation of the organic $[(CH_3)_4P]^+$ cation.

Chlorobismuthate $[Bi_2Cl_9]^{3-}$ anions are also involved in the phase transition as $[(CH_3)_4P]^+$ cations since the Raman bands assigned to the vibration of Bi–Cl bonds (Table 1) also change in position and width at around 80 °C. So, for chlorobismuthate $[Bi_2Cl_9]^{3-}$ anions, the bands observed at 282 and 240 cm^{-1} can be assigned to stretching vibrations of terminal Bi–Cl bonds respectively. The band at 182 and 116 cm^{-1} are attributed to the stretching vibration of equatorial Bi–Cl bonds and to the bending vibration mode of Bi–Cl, respectively (Table S1). All these bands are shifted toward lower wavenumber by 1 cm^{-1} (Fig. 11 a) with a broadening of 2 cm^{-1} (Fig. 11 d) at 80 °C. At the phase transition, the reorientation of the organic $[(CH_3)_4P]^+$ cations is accompanied by a rotation of the $[Bi_2Cl_9]^{3-}$ anions, the former starting 10 °C before the latter as mentioned above. As the movements of the anions and cations are local and progressive, they do not require a large energy input to occur. This explains the absence of an endothermic peak on the DSC curve (Fig. 3) which is characteristic of a second order type transition. Such a behavior has been also observed in the two other chlorobismuthate $(CH_3NH_3)_3Bi_2CI_9$ and $(C_5H_5NH)_6Bi_4Cl_{18}$ [33,34].

3.4.1.2. PCA compound. Fig. 12 shows the temperature dependence of the position and the full width at half maximum (FWHM) for the most intense vibrational bands of PCA compound. As previously mentioned for PCB compound, the vibration modes of (CH_3) are sensitive indicators to phase transition (Fig. 12**a** and **d**). The strongest bands at 2914 and 2990 cm^{-1}, assigned respectively to the symmetric and asymmetric stretching vibrations of methyl group in interaction with the equatorial chlorine atoms, shift in position at 57, 80 and 95 °C concomitantly with the variation of their width. The positions and the widths of the bands associated with the bending vibration modes δ (CH_3) also changes significantly at 57 and 95 °C (Fig. 12b and e). As with PCB, any change in the way the methyl groups vibrate naturally affects the C–P bonds within the C_4P tetrahedron whose the vibration bands are at 649 and 780 cm^{-1}. The difference is that the PCA compound undergoes three successive transitions at 57, 80 and 95 °C, compared to only one for PCB at 70–80 °C.

The bands observed at 314 and 287 cm^{-1} are assigned to stretching vibrations of terminal Sb–Cl bonds and the bands at 241 and 126 cm^{-1} to the stretching vibration modes of equatorial Sb–Cl bonds and bending vibration mode of Sb–Cl, respectively (Table S1). All these bands change abruptly in position at 57, 80 and 95 °C (Fig. 12c) and broaden (Fig. 12f) however a more pronounced broadening is observed for the band at 126 cm^{-1} which starts from 40 °C until the first transition at 57 °C. This behavior is certainly correlated with the structural changes responsible for the broadening of the symmetric and asymmetric stretching vibrations of the methyl group interacting with the terminal chlorine atoms, which incidentally both begin at 30 °C. All these results confirm that the

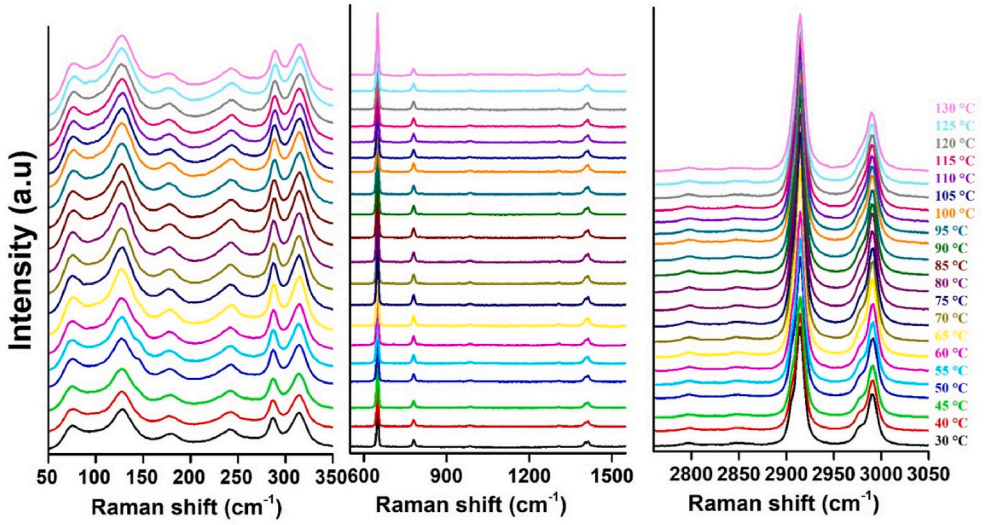

Fig. 10. Temperature evolution ofthe Raman spectra of $[(CH_3)_4P]_3Sb_2Cl_9$ (PCA) compound in the temperature range 30 °C–130 °C for selected spectral ranges [50-350 cm^{-1}], [500-1550 cm^{-1}] and [2750-3050 cm^{-1}].

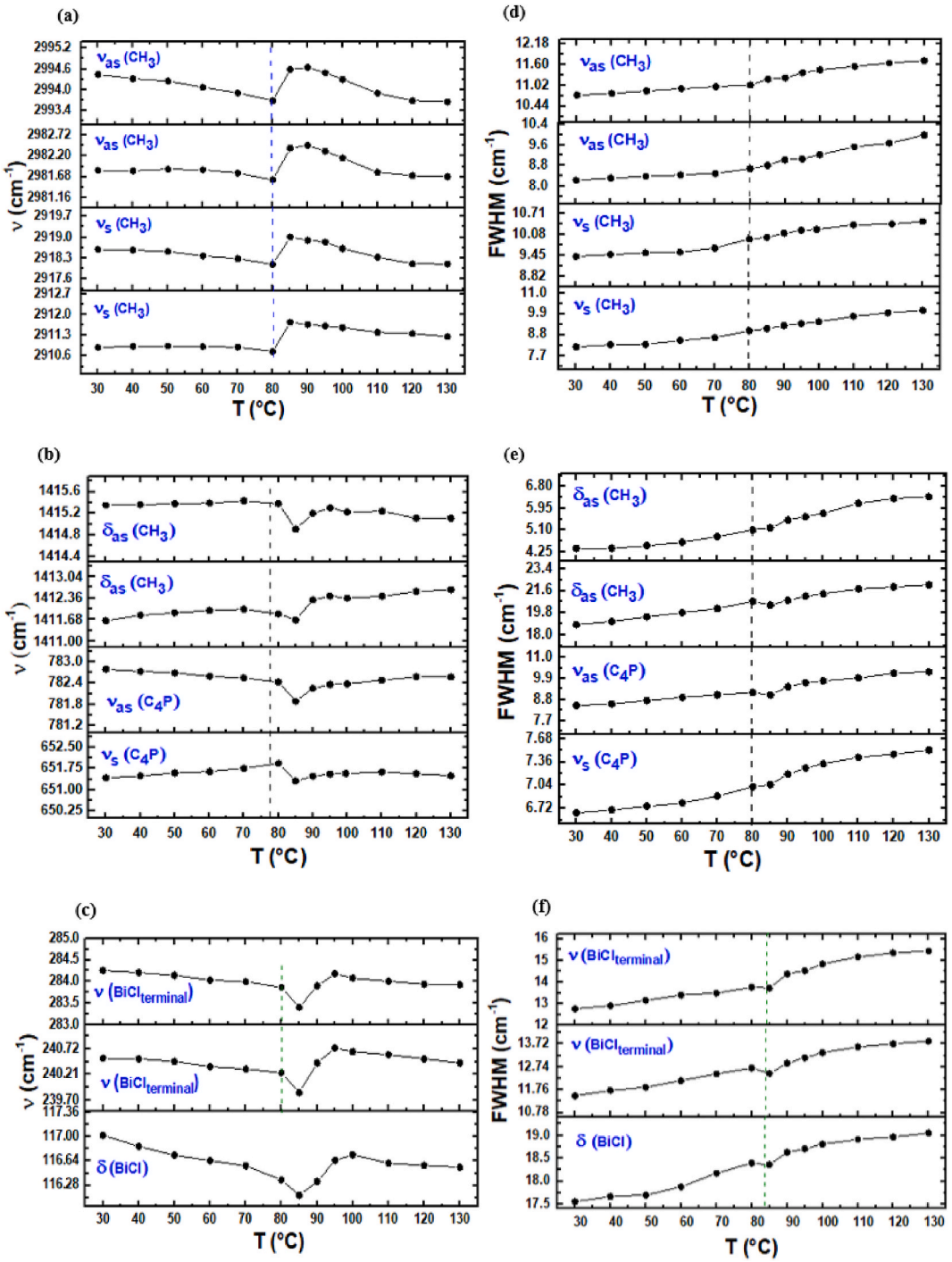

Fig. 11. Temperature evolution of Raman wavenumbers of $[(CH_3)_4P]_3Bi_2Cl_9$ (PCB) in the frequency region assigned to **(a)** the stretching modes of $[Bi_2Cl_9]^{3-}$ anions, **(b)** the asymmetric bending modes of (CH_3) and the stretching modes of (C_4P) and **(c)** the stretching modes of (CH_3). Temperature evolution of full width at half maximum (FWHM) of the Raman bands in the frequency region assigned to **(d)** the stretching modes of $[Bi_2Cl_9]^{3-}$ anions, **(e)** the asymmetric bending modes of (CH_3) and the stretching modes of (C_4P) and **(f)** the stretching vibration modes of (CH_3).

three successive transitions are caused by both reorientations of the organic $[(CH_3)_4P]^+$ cations and rotations of the $[Sb_2Cl_9]^{3-}$ anions, which affects the pattern and maintains the lattice of the crystalline structure.

Thus, for PCA and PCB compounds, we have shown that CH_3 undergoes position and width modifications during phase transitions. In order to complete these Raman analyses, we wanted to verify if the integrated intensities of these vibration bands, and in particular the symmetric and asymmetric stretching vibrations of methyl group in interaction with the terminal chlorine atoms, could be used to highlight the phase transitions. So, we calculated the ratio between the integrated intensity of the symmetric over asymmetric stretching vibrations of methyl (meaning at 2905 cm^{-1} and 2977 cm^{-1}, respectively). Intensity variations are clearly observed around 57, 80 and 92 °C (Fig. S3), suggesting that this method could be applied to other hybrid materials when it is difficult to highlight transitions involving organic components. Finally, let us note that a similar calculation was carried out for the PCB compound and that only one intensity variation at 80 °C was found (Fig. S3).

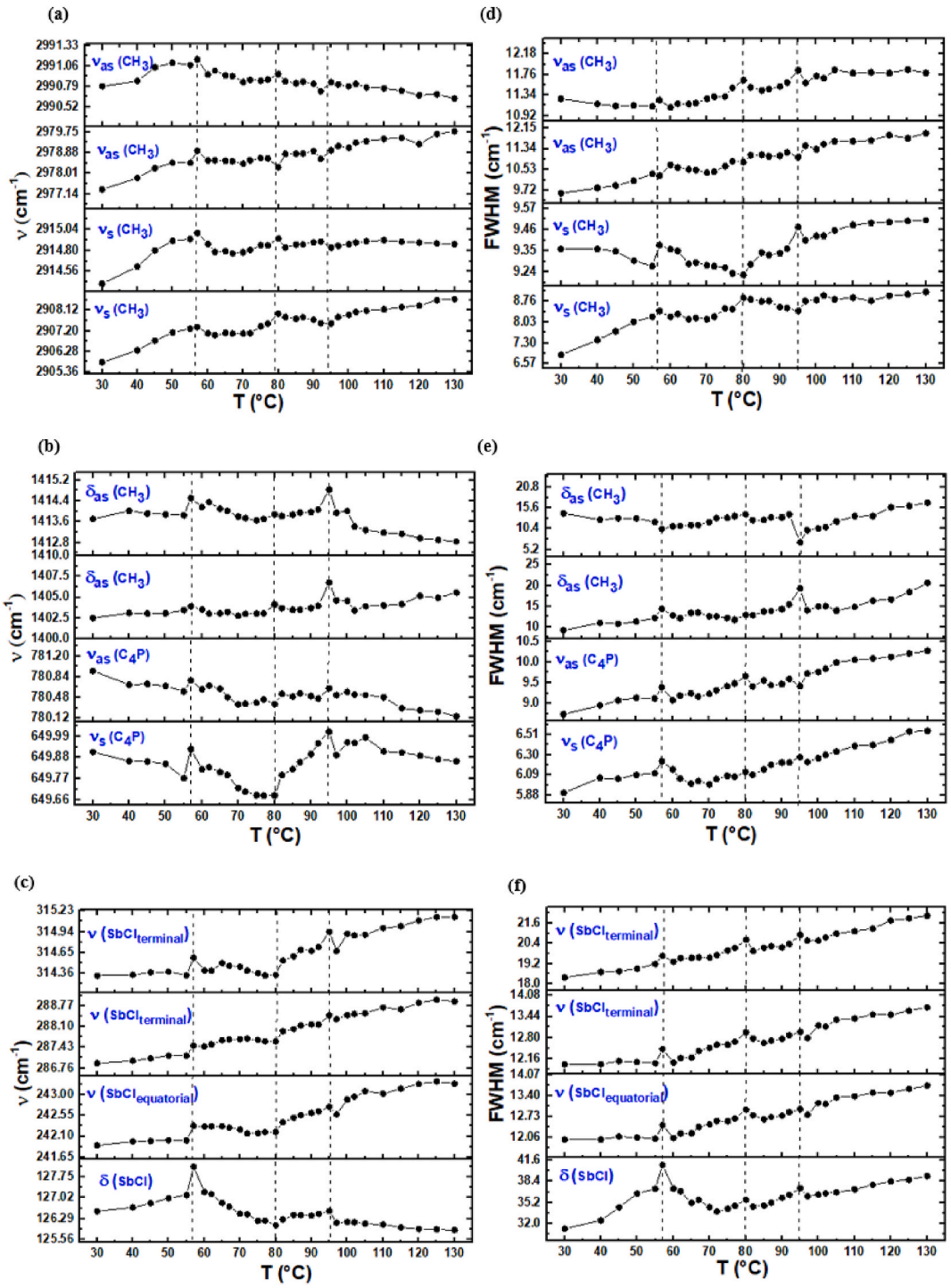

Fig. 12. Temperature evolution of Raman wavenumbers of $[(CH_3)_4P]_3Sb_2Cl_9$ (PCA) in the frequency region assigned to **(a)** the stretching modes of $[Sb_2Cl_9]^{3-}$ anions, **(b)** the asymmetric bending modes of (CH_3) and the stretching modes of (C_4P) and **(c)** the stretching modes of (CH_3). Temperature evolution full width at half maximum (FWHM) of the Raman bands in the frequency region assigned to **(d)** the stretching modes of $[Sb_2Cl_9]^{3-}$ anions, **(e)** the asymmetric bending modes of (CH_3) and the stretching modes of (C_4P) and **(f)** the stretching modes of (CH_3).

3.4.2. X-ray diffraction analysis

In addition to studies by Raman spectroscopy, temperature-controlled X-Ray powder diffraction can provide information about any changes in the crystal structure of PCB and PCA compounds. XRPD patterns collected in air on the both powder PCB and PCA, heated at different temperatures in the range RT to 130 °C, are superimposed in Fig. 13. No change in the shape of diffraction peaks or disappearance/appearance of new ones is noticed on the XRPD patterns collected above 75–80 °C. If the XRPD patterns are comparable in whole temperature range RT – 130 °C, slight and progressive shifts of all diffraction peaks towards low scattering 2θ angles occur as the temperature increases. These shifts are characteristic of a positive thermal expansion of the unit cell parameters. The refinement of each XRPD pattern was carried out by the Le Bail method. For the refinement of the XRPD pattern collected at RT, the trigonal cell parameters, previously determined in section 3.1, were used as starting values. Successively, the trigonal cell parameters

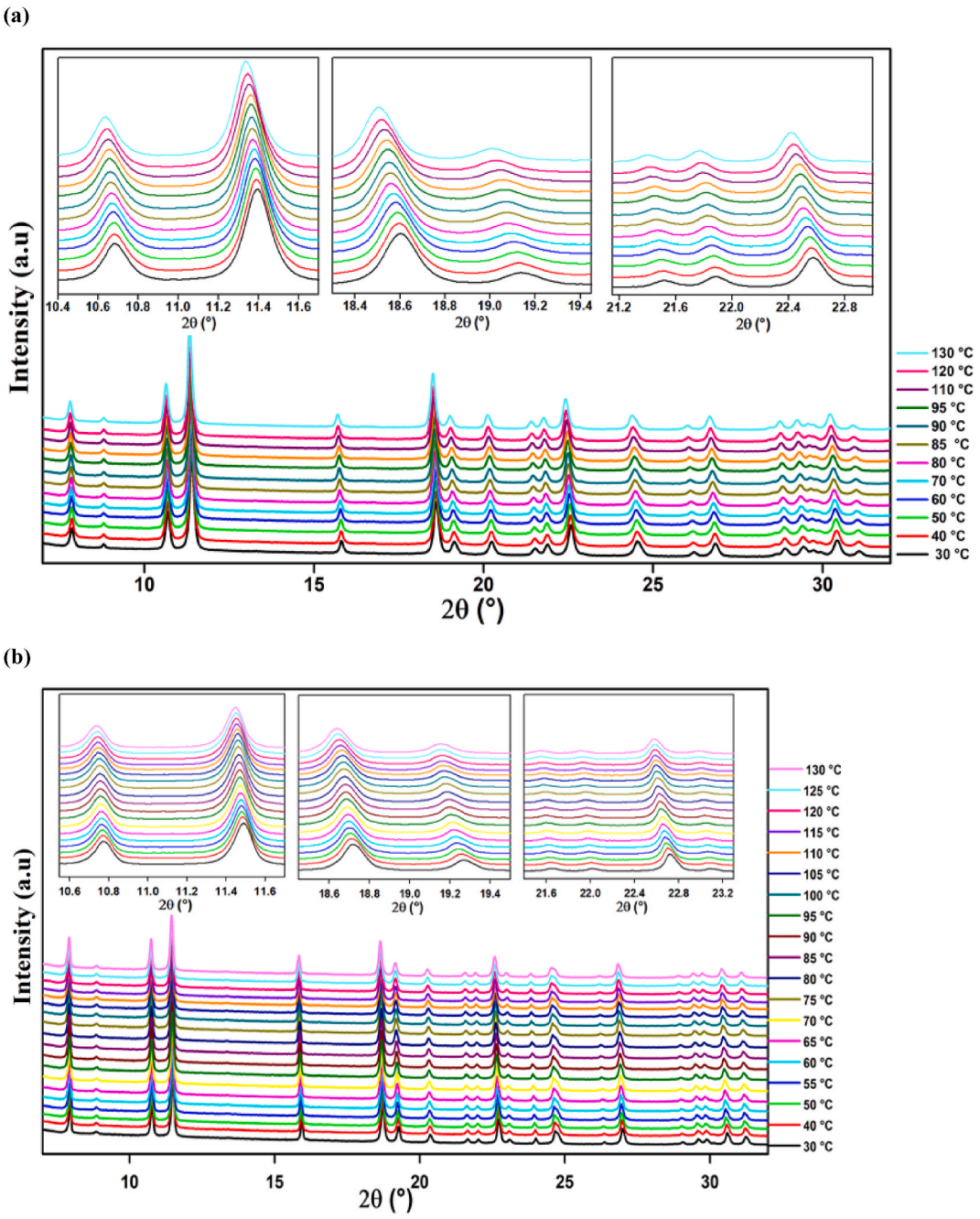

Fig. 13. XRPD patterns collected on the $[(CH_3)_4P]_3Bi_2Cl_9$ (a) and $[(CH_3)_4P]_3Sb_2Cl_9$ (b) powders upon heating in air from RT to 130 °C.

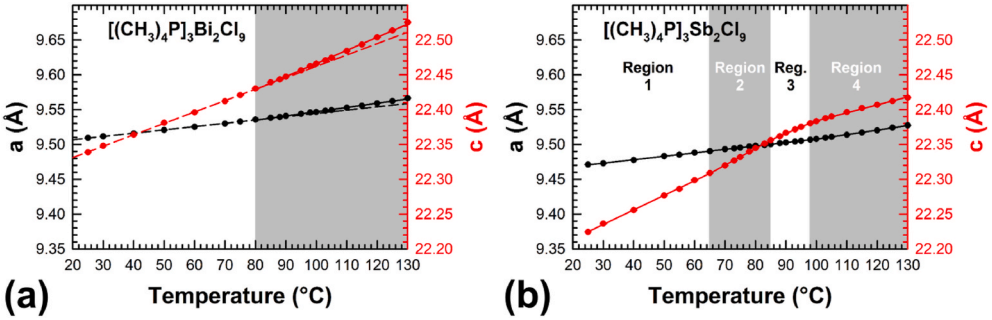

Fig. 14. Thermal evolutions of the trigonal cell parameters a and c determined from the refinement by the Le Bail method of the XRPD patterns of the $[(CH_3)_4P]_3Bi_2Cl_9$ (PCB) (a) and $[(CH_3)_4P]_3Sb_2Cl_9$ (PCA) (b) compounds.

determined from the refinement of a XRPD pattern at each temperature were used as starting values for the refinement of the pattern at the next temperature. All XRPD patterns can be satisfactorily fitted in this way, thus confirming that the trigonal cell of the both crystals structure of PCB and PCA is preserved in the whole temperature range investigated. The thermal evolutions of the cell parameters *a* and *c* of PCB and PCA are displayed in Fig. 14. Fig. 14a shows two thermal domains with linear dependences of each cell parameters of (PCB), corresponding to a small increase in thermal expansion coefficient (TEC) above ≈ 75 °C. The thermal expansions coefficients along the *a* crystallographic axis is 4.64 × 10^{-4} °C^{-1} and 5.87 × 10^{-4} °C^{-1} in the range RT-75 °C and 75–130 °C, respectively. The thermal expansion coefficients along the *c* crystallographic axis are 1.62 × 10^{-3} °C^{-1} and 1.84 × 10^{-3} °C^{-1} in the range RT-75 °C and 75–130 °C, respectively.

Fig. 14b shows two thermal domains with linear dependences of each cell parameters of (PCA), corresponding to increase in thermal expansion coefficient above ≈ 65, 85 and 95 °C. Whatever the thermal domains considered, the thermal expansion along the [001] direction is much larger in magnitude than the one in the basal (*a,b*) plane. Both changes in TEC concomitantly occur with the discontinuities in the thermal evolution of the vibrational modes associated with the tetramethyl phosphonium $[(CH_3)_4P]^+$ cations. This suggests that the discontinuities in the thermal evolution of the vibrational modes and changes in TEC around 80 °C for PCB and 65, 85 and 95 °C for PCA, are due to smaller orientations of the tetramethyl phosphonium cations $[(CH_3)_4P]^+$ and rotations of $[M_2Cl_9]^{3-}$ dimers in the crystal structure. This explains why these new phase transitions are of second order.

When six-fold coordinated to anions, trivalent antimony is slightly smaller in size that trivalent bismuth [35]. This difference in size explains why the unit cell parameters *a* and *c* for PCA are also smaller than that for PCB (Fig. 14). Because of this reduction in cell volume, we believe that reorientations of the tetramethyl phosphonium cations $[(CH_3)_4P]^+$ and rotations of $[Sb_2Cl_9]^{3-}$ dimers in the structure of PCA are not as easy as in the structure of PCB. This could explain that these movements take place in three successive steps and not in a single step as in PCB.

4. Conclusion

In this paper, the $[(CH_3)_4P]_3Bi_2Cl_9$ (PCB) and $[(CH_3)_4P]_3Sb_2Cl_9$ (PCA) compounds have been synthesized by slow evaporation method at room temperature. The structural refinement confirms that both compounds crystallize in the trigonal system with a space group of *P31c*. Raman and XRD studies reveal that the structure of PCB and PCA crystals start to decompose above 250 °C. The SEM image and the EDX analysis show the inhomogeneity of both crystals surface and the increases of proportion of carbon and oxygen after heating (above 270 °C). The analysis of the positions and widths of the vibration bands of PCB and PCA compounds, as a function of the heating temperature, allowed us to highlight specific temperatures which can be assigned to phase transitions based on a dynamical reorientation of the organic $[(CH_3)_4P]^+$ cations with a rotation of $[M_2Cl_9]^{3-}$ anions (M = Bi or Sb). The behavior of the thermal evolutions, which shows a slope change of the cell parameters *a* and *c* of both compounds confirmed the presence of the new phase transitions detected by Raman spectroscopy. PCB exhibits only one phase transition at 80 °C while 3 successive phase transitions at about 60, 80 and 95 °C are detected for PCA. The number of transitions may be related to the free volume available for reorientations of the tetramethyl phosphonium cations $[(CH_3)_4P]^+$ and rotations of $[M_2Cl_9]^{3-}$ dimers in the unit cell, this free volume being smaller in PCA than in PCB.

CRediT authorship contribution statement

Mariem KHALFA: Investigation (Raman Spectroscopy and Diffraction), Writing- Original draft and Writing - Review & Editing. Abderrazek OUESLATI: Writing- Original draft. Kamel KHIROUNI: Writing- Original draft- Review & Editing. Mohamed GARGOURI: Writing- Original draft. Anthony ROUSSEAU: Investigation (Scanning Electron Microscopy). Jean-François BARDEAU: Investigation, Formal analysis and Data Curation (Raman Spectroscopy), Writing- Original draft, Writing - Review & Editing. Gwenaël CORBEL: Investigation, Formal analysis and Data Curation (Thermal analyses and Diffraction), Writing- Original draft, Writing - Review & Editing.

Declaration of competing interest

The authors declare that they have no known competing financial interests or personal relationships that could have appeared to influence the work reported in this paper.

Data availability

Data will be made available on request.

Acknowledgment

This work was funded by the Tunisian Ministry of Higher Education and Scientific Research and French Ministry of Higher Education and Research through funds accorded to the implied research Labs.

Appendix A. Supplementary data

Supplementary data to this article can be found online at https://doi.org/10.1016/j.jpcs.2023.111227.

References

[1] M. Wojtaś, R. Jakubas, Structure and properties of $[(CH_3)_4P]_3$ $[Sb_2Cl_9]$ and $[(CH_3)_4P]_3[Bi_2Cl_9]$, J. Phys. Condens. Matter 16 (2004) 7521–7534, https://doi.org/10.1088/0953-8984/16/41/029.

[2] A.S. Rao, U. Baruah, S.K. Das, Stabilization of $[BiCl_6]^{3-}$ and $[Bi_2Cl_{10}]^{4-}$ with various organic precursors as cations leading to inorganic–organic supramolecular adducts: syntheses, crystal structures and properties of $[C_5H_7N_2]_3[BiCl_6]$, $[C_5H_7N_2][C_5H_8N_2][BiCl_6]$ and $[C_{10}H_{10}N_2]_2[Bi_2Cl_{10}]$, Inorg. Chim. Acta. 372 (2011) 206–212, https://doi.org/10.1016/J.ICA.2011.01.109.

[3] R. Jakubas, A. Piecha, A. Pietraszko, G. Bator, Structure and ferroelectric properties of $(C_3N_2H_5)$ $_5Bi_2Cl_{11}$, Phys. Rev. B 72 (2005), 104107, https://doi.org/10.1103/PhysRevB.72.104107.

[4] M. Wojtaś, R. Jakubas, J. Baran, Vibrational study of the ferroelastic phase transition in $[(CH_3)_4P]_3[Bi_2Cl_9]$ and $[(CH_3)_4P]_3[Bi_2Br_9]$, Vib. Spectrosc. 39 (2005) 23–30, https://doi.org/10.1016/J.VIBSPEC.2004.10.004.

[5] M. Wojtaś, R. Jakubas, Z. Ciunik, W. Medycki, Structure and phase transitions in $[(CH_3)_4P]_3[Sb_2Br_9]$ and $[(CH_3)_4P]_3[Bi_2Br_9]$, J. Solid State Chem. 177 (2004) 1575–1584, https://doi.org/10.1016/J.JSSC.2003.12.011.

[6] B. Zarychta, J. Zaleski, Phase transitions mechanism and distortion of $SbCl_6^{3-}$ octahedra in Bis(n-butylammonium) Pentachloroantimonate(III) $(C_4H_9NH_3)_2[SbCl_5]$, Z. Naturforsch. B Chem. Sci. 61 (2006) 1101–1109, https://doi.org/10.1515/znb-2006-0908.

[7] M.R. Pressprich, M.R. Bond, R.D. Willett, Structures of $[(CH_3)_4P]_2CoCl_4$, $[(CH_3)_4Sb]_2CuCl_4$ and $[(CH_3)_4Sb]_2ZnBr_4$ and a correlation of pseudo-antifluorite $[(CH_3)_4P]_2MX_4$ salts, J. Phys. Chem. Solid. 63 (2002) 79–88, https://doi.org/10.1016/S0022-3697(01)00081-6.

[8] P. Szklarz, R. Jakubas, A. Piecha-Bisiorek, G. Bator, M. Chański, W. Medycki, J. Wuttke, Organic-inorganic hybrid crystals, (2,4,6-$CH_3PyH)_3Sb_2Cl_9$ and (2,4,6-$CH_3PyH)_3Bi_2Cl_9$. Crystal structure characterization and tunneling of CH3 groups studied by ^{1}H NMR and neutron spectroscopy, Polyhedron 139 (2018) 249–256, https://doi.org/10.1016/J.POLY.2017.10.030.

[9] S.A. Nedil'ko, I.V. Fesych, O.G. Dzyazko, A.S. Bulachok, S.O. Solopan, T. O. Plutenko, Synthesis of barium cuprate by secondary induction heating and its electrical properties, Powder Metall. Met. Ceram. 55 (2016) 347, https://doi.org/10.1007/s11106-016-9812-1.

[10] I. Tmar Trabelsi, A. Oueslati, T. Mhiri, M. Toumi, Synthesis, characterization and ionic conductivity of $Ca_{8-x}Sr_xBi_2(PO_4)_6O_2$ for x = {3, 4, 5, J. Alloys Compd. 641 (2015) 14–21, https://doi.org/10.1016/J.JALLCOM.2015.04.055.

[11] L. Sobczyk, R. Jakubas, J. Zaleski, Self-assembly of Sb(III) and Bi(III) halo-coordinated octahedra in salts of organic cations. Structure, properties and phase transitions, Pol. J. Chem. 71 (1997) 265–300.

[12] C.R. Kagan, D.B. Mitzi, C.D. Dimitrakopoulos, Organic-inorganic hybrid materials as semiconducting channels in thin- film field-effect transistors, Science 286 (1999) 945–947, https://doi.org/10.1126/science.286.5441.945.

[13] Jean-Claude Toledano, La ferroélasticité, Ann. Des Télécommun. 29 (1974) 249–270, https://doi.org/10.1007/BF02996935.
[14] P.-P. Shi, Q. Ye, Q. Li, H.-T. Wang, D.-W. Fu, Y. Zhang, R.-G. Xiong, Novel phase-transition materials coupled with switchable dielectric, magnetic, and optical properties: $[(CH_3)_4P][FeCl_4]$ and $[(CH_3)_4P][FeBr_4]$, Chem. Mater. 26 (2014) 6042–6049, https://doi.org/10.1021/cm503003f.
[15] H. Elgahami, W. Trigui, A. Oueslati, J. Lhoste, F. Hlel, Crystal structure, Hirshfeld surface analysis, Thermal study and Conduction mechanism of $[(C_4H_9)_4P]_3Bi_2Cl_9$ compound, Appl. Organomet. Chem. 33 (2019) e5078, https://doi.org/10.1002/aoc.5078.
[16] R. Megha, S. Kotresh, Y.T. Ravikiran, C.V.V. Ramana, S.C. Vijaya Kumari, S. Thomas, Study of alternating current conduction mechanism in polypyrrole-magnesium ferrite hybrid nanocomposite through correlated barrier hopping model, Compos. Interfac. 24 (2017) 55–68, https://doi.org/10.1080/09276440.2016.1185298.
[17] M. Ben Gzaiel, A. Oueslati, I. Chaabane, A. Bulou, F. Hlel, M. Gargouri, Using Raman spectroscopy to understand the origin of the phase transitions observed in $[(C_3H_7)_4N]_2Zn_2Cl_6$ compound, Spectrochim. Acta Part A Mol. Biomol. Spectrosc. 145 (2015) 223–234, https://doi.org/10.1016/J.SAA.2015.02.102.
[18] A. Le Bail, H. Duroy, J.L. Fourquet, Ab-initio structure determination of $LiSbWO_6$ by X-ray powder diffraction, Mater. Res. Bull. 23 (1988) 447–452, https://doi.org/10.1016/0025-5408(88)90019-0.
[19] J. Rodríguez-Carvajal, Recent advances in magnetic structure determination by neutron powder diffraction, Phys. B Condens. Matter 192 (1993) 55–69, https://doi.org/10.1016/0921-4526(93)90108-I.
[20] K. Nakamoto, Infrared and Raman Spectra of Inorganic and Coordination Compounds, Part B: Applications in Coordination, Organometallic, and Bioinorganic Chemistry, John Wiley & Sons, 2009.
[21] V. Varma, R. Bhattacharjee, H.N. Vasan, C.N.R. Raot, Infrared and Raman spectroscopic investigations of methylammonium haloantimonates(III), $[N(CH_3)_{4-n}H_n]$, Sb_2X_9 (n = 0-3, X = Cl or Br), through their phase transitions, Spectrochim. Acta 48A (1992) 1631–1646, https://doi.org/10.1016/0584-8539(92)80237-Q.
[22] F.-J. Kruger, F. Zettler, A. Schmidt, Tri- und TetraMethylammonium-chloroantimonate(III), Z. Anorg. Allg. Chem. 449 (1979) 135–144, https://doi.org/10.1002/zaac.19794490114.
[23] M. Wojtaś, G. Bator, J. Baran, Vibrational study of structural phase transitions in $[(CH_3)_2NH_2]_3[Bi_2Cl_9]$ and $[(CH_3)_2NH_2]_3[As_2Cl_9]$ crystals, Vib. Spectrosc. 33 (2003) 143–152, https://doi.org/10.1016/J.VIBSPEC.2003.07.001.
[24] S. Shamaila, A.K.L. Sajjad, F. Chen, J. Zhang, WO_3/BiOCl, a novel heterojunction as visible light photocatalyst, J. Colloid Interface Sci. 356 (2011) 465–472, https://doi.org/10.1016/J.JCIS.2011.01.015.
[25] R. Sarkar, D. Das, A. Mitra, S. Sarkar, K.K. Chattopadhyay, Faceted growth of morphologically tuned of BiOCl, Mater. Today Proc. 18 (2019) 1086–1095, https://doi.org/10.1016/J.MATPR.2019.06.568.
[26] G. Mestl, P. Ruiz, B. Delmon, H. Knozinger, Sb_2O_3/Sb_2O_4 in reducing/oxidizing environments: an in situ Raman spectroscopy study, J. Phys. Chem. 98 (1994) 11276–11282, https://doi.org/10.1021/j100095a008, 1994.
[27] P.I.R.K.G. Keramidas, G.P. Voutsas, The crystal structure of BiOCl, Z. für Kristallogr. - Cryst. Mater. 205 (1993) 35–40, https://doi.org/10.1524/zkri.1993.205.Part-1.35.
[28] M. Khalfa, A. Oueslati, K. Khirouni, M. Gargouri, A. Rousseau, J. Lhoste, J.-F. Bardeau, G. Corbel, Synthesis, structural and electrical characterization of a new organic inorganic bromide: $[(C_3H_7)_4N]_2CoB_4$, RSC Adv. 12 (2022) 2798–2809, https://doi.org/10.1039/d1ra07965d.
[29] W. Trigui, F. Hlel, Ferroelectric properties and Raman spectroscopy of the $[(C_4H_9)_4N]_3$ Bi_2 Cl_9 compound, RSC Adv. 9 (2019) 24291–24298, https://doi.org/10.1039/c9ra02577d.
[30] W. Trigui, A. Oueslati, F. Hlel, A. Bulou, Raman study of order-disorder phase transition in $[(C_3H_7)_4N]_3Bi_3Cl_{12}$ compound, J. Mol. Struct. 1106 (2016) 19–29, https://doi.org/10.1016/J.MOLSTRUC.2015.10.071.
[31] R.L. Moreira, F.M. Matinaga, A. Dias, Raman-spectroscopic evaluation of the long-range order in $Ba(B_{1/3}'B_{2/3}'')O_3$ ceramics, Appl. Phys. Lett. 78 (2001) 428–430, https://doi.org/10.1063/1.1339254.
[32] K. Ben Brahim, M. Ben, A. Oueslati, K. Khirouni, M. Gargouri, G. El Corbel, J.-F. Bardeau, Organic-inorganic interactions revealed by Raman spectroscopy during reversible phase transitions in semiconducting $[(C_2 H_5)_4N]FeCl_4$, RSC Adv. 11 (2021) 18651–18660, https://doi.org/10.1039/d1ra02475b.
[33] I. Belkyal, R. Mokhlisse, B. Tanouti, N.B. Chanh, M. Couzi, X-ray diffraction and Raman scattering in $(CH_3NH_3)_3Bi_2Cl_9$ (MACB) single crystals, Phys. Status Solidi 136 (1993) 45–56, https://doi.org/10.1002/pssa.2211360105.
[34] J. Tarasiewicz, R. Jakubas, J. Baran, Raman studies of the anionic sublattice vibrations in $(C_5H_5NH)_6Bi_4Cl_{18}$, J. Mol. Struct. 614 (2002) 333–338, https://doi.org/10.1016/S0022-2860(02)00268-5.
[35] R.D. Shannon, IUCr, Revised effective ionic radii and systematic studies of interatomic distances in halides and chalcogenides, Acta Crystallogr. A 32 (1976) 751–767, https://doi.org/10.1107/S0567739476001551.